"POLITEHNICA" UNIVERSITY OF BUCHAREST

ETTI-B DOCTORAL SCHOOL

Contributions to the development of navigation and communication techniques for satellite constellations

Summary

PhD Student Eng. Alexandru Mihai Crişan
Advisor Prof. Dr. Eng. Daniela Colţuc

Bucharest 2020

Contents

List of abbreviations

AoA - Angle-of-Arrival

AWGN - Additive White Gaussian Noise

CFO - Carrier Frequency Offset

CLS - Coarse Lateral Sensor

CP - Cyclic Prefix

DC - Direct Current

DDC - Digital Downconverter

DFT - Discrete Fourier Transform

DL - Downlink

DOWR - Dual One-Way Ranging

DUC - Digital Upconverter

EWL - Enhanced Wide-lane

FFO - Fractional Frequency Offset

FFRF - Formation Flying Radio Frequency

FFT - Fast Fourier Transform

FIFO - First In First Out

FLLS - Fine Lateral and Longitudinal Sensor

FPGA - Field-programmable Gate Array

GNSS - Global Navigation Satellite System

GPS - Global Positioning System

HCR - Half-Cycle Rounding

I/Q - In-phase and Quadrature

ICI - Inter-Carrier Interference

IDFT - Inverse Discrete Fourier Transform

IFFT - Inverse Fast Fourier Transform

IFO - Integer Frequency Offset

ISI - Inter-Symbol Interference

ISL - Inter-Satellite Link

KBR - K-Band Ranging

LMMSE - Linear Minimum Mean Squarred Error

LoS - Line-of-Sight

LS - Least Squares

LTE - Long Term Evolution

MS - Master Satellite

MSE - Mean Squared Error

OFDM - Orthogonal Frequency-Division Multiplexing

OSC - Occulter Spacecraft

PAPR - Peak-to-Average Power Ratio

PFF - Precision Formation Flying

QPSK - Quaternary Phase-Shift Keying

RF - Radio Frequency

SFO - Sampling Frequency Offset

SNR - Signal-to-Noise Ratio

SS - Slave Satellite

TDD - Time Division Duplexing

TDX - TanDEM-X

TSX - TerraSAR-X

UL - Uplink

USRP - Universal Software Radio Peripheral

ZC - Zadoff-Chu

Chapter 1

Introduction

Future space missions require the deployment of large-scale scientific instruments distributed across multiple spacecraft. The practical approach to implement this type of technology is precision formation flying (PFF). In PFF, the satellites that form the constellation cooperate using inter-satellite links (ISL) to achieve their goals. In order to perform the virtual structure build-up required by the scientific mission, accurate information regarding the relative positioning of the satellites in terms of distance and orientation becomes mandatory. For space missions that cannot rely on the coverage of Global Positioning System (GPS), high-precision optical or radio frequency (RF) metrology systems that can accomodate multiple satellites must be developed. Although the optical systems have higher accuracy, the RF techniques have the advantage that they do not require dedicated hardware because the ISL can also be used for the metrology measurements. This thesis is focused on RF systems for inter-satellite communications that also perform the required metrology measurements. The original contributions, consisting in newly developed techniques for ISL synchronization and metrology, are presented in the context of a formation composed of two satellites. The new techniques can easily be scaled to accomodate several spacecraft.

Chapter 2

State-of-the-art Formation Flying

This chapter presents several space missions, either already launched or under development, that employ aspects of formation flying. The presented missions use RF techniques, optical solutions or a combination of both for metrology measurements and constitute relevant examples for relative navigation or positioning.

2.1 TanDEM-X

The first mission to employ satellite formation flying technologies is TanDEM-X. It is an Earth Observation mission based on two nearly identical satellites, TerraSAR-X (TSX) and TanDEM-X (TDX), that fly in close formation to achieve interferometric baselines in a highly reconfigurable constellation [1]. The goals of the mission are to generate a global high precision digital elevation model and to provide a configurable Synthetic Aperture Radar interferometry platform. Each satellite is equipped with two GPS receivers: the dual-frequency IGOR GPS receiver has scientific purposes exclusively, and the single frequency MosaicGNSS receiver which is used by the formation flying system [2].

Two ISLs are implemented on the satellites. One is in the X-band and is used for phase referencing between TSX and TDX. The second ISL is in S-band and is designed to work for distances up to 5 km and is used to broadcast GPS data from TSX to TDX. The S-band receiver on TDX provides a one-way link to receive real-time position and velocity data from the GPS receiver on TSX.

2.2 GRACE

Gravity Recovery And Climate Experiment (GRACE) is a space mission whose main objective is to map the Earth's gravity field. The mission is implemented utilizing a formation of two identical satellites, whose orbits are affected differently by gravitational and non-gravitational accelerations, leading to changes in the inter-satellite distance. These changes are monitored with the K-Band Ranging (KBR) microwave tracking system and are used to model the gravity field [3].

KBR is a Dual One-Way Ranging (DOWR) instrument [4] developed by the Jet Propulsion Laboratory that employs carrier phase measurements in the K (26 GHz) and Ka (32 GHz) bands. Each satellite transmits a carrier in the respective bands towards the other spacecraft. Then, each satellite measures the carrier phases of the received signals using phase-locked loops, assigns a timestamp provided by the onboard GPS receiver and proceeds to transmit the measurements towards the ground station.

2.3 PRISMA

Prototype Research Instruments and Space Mission technology Advancement (PRISMA) is a satellite formation flying mission consisting in two spacecraft: the primary satellite, called MAIN has maneuvering capabilities; the secondary satellite, called TARGET, is the positioning reference for MAIN and follows the preset orbital trajectory. The main objective of the mission is to demonstrate formation flying and rendezvous technologies. To this end several sensors have been employed: a GPS system, a Vision Based Sensor and a Formation Flying Radio Frequency (FFRF) sensor. The MAIN satellite will adjust its trajectory around the second spacecraft based on the information received from the sensors. The bidirectional ISL is in the 450 MHz band, has a symmetrical data rate of 19.2 kbps and can operate for distances up to 10 km [5].

FFRF is a radio-frequency metrology sensor that can provide relative positioning in terms of distance, orientation and velocity for up to four satellites flying in formation [6]. The system operates in the S-band and the satellites can communicate with eachother using a Time Division Multiple Access (TDMA) scheme. An ISL can also be provided with a data rate of up to 12 kbps.

2.4 PROBA-3

Project for On-Board Autonomy-3 (PROBA-3) is the European Space Agency's first PFF mission. PROBA-3 will be launched in 2020 with the goal of demonstrating satellite formation flying technologies in the context of a large scale scientific experiment. The mission is implemented using two satellites that will maintain a fixed configuration in order to form a 150-m long solar coronagraph.

The RF system used in PROBA-3 is GAMALINK, a software defined radio communications and networking platform. It has the capability of GPS navigation, while also supporting precise ranging measurements [7]. The frequency range of the platform is 0.3-3 GHz with an instantaneous bandwidth of up to 40 MHz. The maximum supported data rate is 80 Mbps and the accuracy of GPS positioning is 5 m. Other dedicated metrology instruments are the Coarse Lateral Sensor (CLS) and the Fine Lateral and Longitudinal Sensor (FLLS).

Chapter 3

Orthogonal Frequency-Division Multiplexing

This chapter is dedicated to the analysis of the Orthogonal Frequency-Division Multiplexing (OFDM) communication system, viewed as a solution for the ISL implementation. In this chapter two channel estimation techniques are analyzed and evaluated by means of MATLAB simulations. The impact of ionospheric scintilation on the channel model is also discussed.

3.1 OFDM concept

In OFDM the digital data is transmitted on multiple carrier frequencies, called subcarriers. OFDM is used in wideband digital communications such as digital television broadcasting, wireless networks and Long-Term Evolution (LTE, Fourth Generation mobile communications). The advantages that make OFDM a prime candidate for ISLs are high spectral efficiency, robustness against narrow-band effects, inter-symbol interference (ISI) and fading and simple channel equalization.

3.1.1 Effects of timing and frequency offsets

At the receiver, since the time scale is unknown, the beginning of the OFDM symbol or radio frame that contains multiple symbols must be identified in order to correctly position the Discrete Fourier Transform (DFT) window for data demodulation. A timing error leads to both inter-carrier interference (ICI) and ISI.

In inter-satellite communications, the differences between the local oscillators of the transmitter and receiver and the Doppler effect give rise to a shift in the frequency domain. This shift is referred to as *carrier frequency offset* (CFO). The CFO is split into a fractional frequency offset (FFO) and an integer frequency offset (IFO). In OFDM, the demodulation of a signal with an offset in the carrier frequency leads to orthogonality loss, ICI and large bit error rates.

Another disturbance in OFDM systems is the sampling clock mismatch between transmitter and receiver. In time-domain, the sampling frequency offset (SFO) leads to a symbol window drift. Although this is a long-term effect, procedures must be in place to account for it. In the frequency domain SFO introduces ICI and a phase rotation of the received constellations. Since ICI is treated as additional noise, only the phase rotation must be compensated.

The SFO can be estimated using techniques such as frequency domain correlation of consecutive and identical OFDM symbols [8] or pilot sub-carrier phase drift estimation [9].

3.2 Multipath propagation and channel estimation

Reflecting objects and scatterers in the channel lead to a changing propagation environment, which in turn causes variations in the signal amplitude, phase and time delay. The most important effects of multipath are rapid variations in signal power, frequency modulation caused by Doppler shifts on different echoes and time dispersion due to the relative delays of the multipath signals.

The use of the CP allows the convolution between the transmitted signal $x[n]$ and the channel impulse response $h[n]$ to be modeled as circular convolution. This is equivalent to pointwise multiplication in the frequency domain [10]:

$$Y_{mp}[k] = X[k]H[k] \tag{3.1}$$

where $Y_{mp}[k]$ is the DFT of the received signal and $H[k]$ is the channel transfer function.

I tested the least squares (LS) and simplified linear minimum mean-squared error (LMMSE) estimators by simulations under MATLAB. For simulations I considered the DFT size $N = 512$, the CP length $N_{CP} = 36$ samples and a channel with 3 taps. In order to estimate the channel, a preamble consisting in one training symbol with 300 active sub-carriers is used. The SNR is varied from 0 to 35 dB and 2500 runs are performed at each SNR. The mean squared error (MSE) of the channel estimation is plotted in Fig. 3.3. It can be seen that the modified LMMSE estimator significantly outperforms the basic LS estimator. At a SNR of 10 dB, the error for LS is 0.19, while the error for LMMSE is $3 \cdot 10^{-4}$.

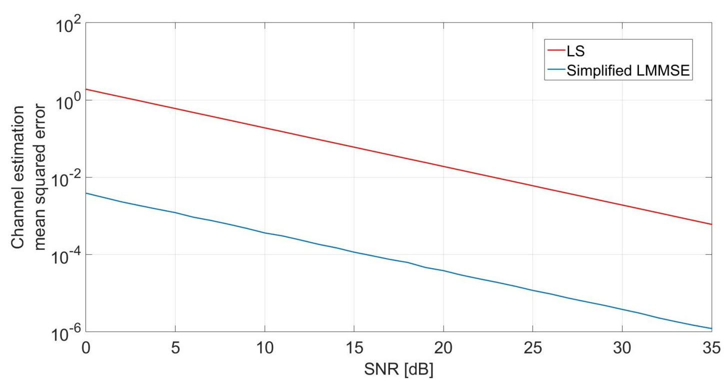

Figure 3.3: MSE values of channel estimators vs. SNR obtained from simulations.

3.3 Ionospheric scintillation

Ionospheric scintillation is a rapid fluctuation of the RF signal amplitude and phase when it passes through the ionosphere. The instability of the irregularities and the ionization of the medium generate turbulences in the ionosphere that influence the radio wave propagation [11]. Some of the effects of ionospheric scintillation include Faraday rotation and increased group delay of radio waves, dispersion and change in angle-of-arrival (AoA).

Scintillation intensity is modeled by the S_4 index [11] and can be classified into three regimes: weak ($S_4 < 0.3$), moderate ($0.3 \leq S_4 \leq 0.6$) and strong scintillation ($S_4 > 0.6$).

Table 3.2 shows the maximum estimated values of the ionospheric effects for a 2 GHz radio wave [12]. P_{fluc} represents the peak-to-peak fluctuations of received signal power in dB and σ_φ is the standard deviation of the phase fluctuations. The values correspond to one-way propagation.

Table 3.2: Maximum values of ionospheric effects for a 2 GHz signal

Effect	Faraday rotation	Group delay	Refraction	AoA variation	Absorption	Dispersion	P_{fluc}	σ_φ
Value	0.02°	$<$ 500 ps	0.04 mrad	0.04 min	0.01 dB	1 ns/MHz	6 dB	0.3 rad

Chapter 4

Time and frequency synchronization in OFDM systems

This chapter is focused on synchronization techniques for OFDM systems. It starts with the presentation of several timing and fractional frequency offset (FFO) estimation techniques, then the novel ISL synchronization algorithm developed in during the doctoral studies is presented. The original contributions on the subject of synchronization are:

- An analysis of three timing and FFO estimation techniques in order to identify a suitable solution for ISLs (results published in [13]);
- The development of a novel ISL synchronization algorithm that achieves fine timing and does not require an IFO estimator [14].

4.1 Timing and fractional CFO estimation

The baseband samples of the generated OFDM symbol can be expressed as [15]:

$$x[n] = \frac{1}{\sqrt{N}} \sum_{k=-N/2}^{N/2+1} d[k] e^{j2\pi nk/N} \tag{4.1}$$

where N is the IDFT size. In the case of a training symbol, a Zadoff-Chu (ZC) sequence can be used to generate the complex values $d[k]$. ZC sequences have constant amplitude and the cyclically shifted versions do not cross-correlate with one another.

Transmitting the signal through an additive white gaussian noise (AWGN) channel leads to the following baseband signal form at the receiver [16]:

$$y[n] = x[n - \Delta n] e^{j2\pi n \frac{\Delta F_c}{F_s}} \tag{4.2}$$

where Δn is the timing offset, F_s is the sampling frequency and the FFO is modeled by the phasor $e^{j2\pi n \frac{\Delta F_c}{F_s}}$.

4.1.1 Simulation results

The performances of three timing and FFO estimation techniques, namely Schmidl-Cox [15], cyclic prefix (CP) autocorrelation [16] and cross-correlation, are evaluated by means of MATLAB simulations. The results of this comparison have been published in [13]. The following simulation parameters are used: $N = 64$, $F_s = 0.5$ MHz, $\Delta n = 100$ and $\Delta F_c = 524$ Hz. Four 3 dB attenuated channel taps around the correct starting point of the preamble are considered. At each SNR 2500 runs are performed.

The expectation values of the timing offset estimations are plotted in Figure 4.3. The correct values corresponding to each technique are written between parentheses.

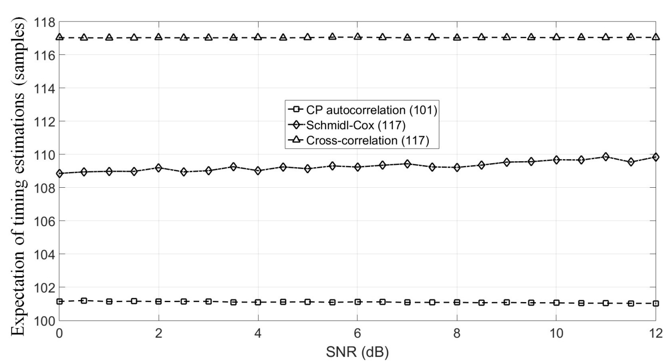

Figure 4.3: Expectation of timing offset estimations vs. SNR obtained from simulations. The correct values are written between parentheses.

It can be seen that all three estimators are biased. The CP autocorrelation provides accurate estimates and the bias is one sample. For the cross-correlation method, fine timing is achieved (the FFO is well within range) and the bias is equal to $N_{CP} + 1$, where N_{CP} is the CP length. For Schmidl-Cox, the expectation is approximately 109 samples, so the bias is 9 samples. This suggests that the correct sample index 117 would be indicated if the estimated values were advanced by $N_{CP}/2$ samples.

The standard deviations of the timing offset estimations are shown in Figure 4.4. For the cross-correlation method, the values are practically constant with SNR. For CP autocorrelation, the standard deviation becomes smaller as the SNR increases. The Schmidl-Cox method has high errors because of the plateau in the timing metric.

The expectations of the three FFO estimators are compared in Figure 4.5. The

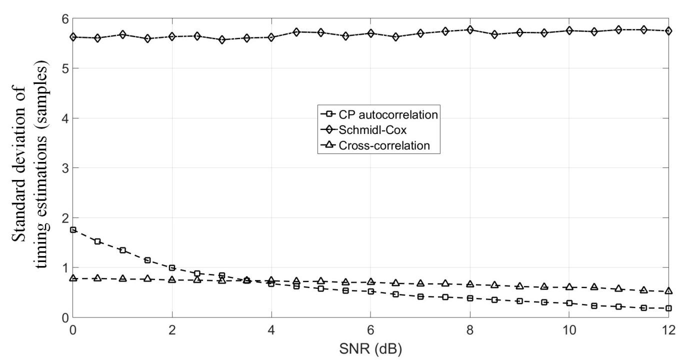

Figure 4.4: Standard deviation of timing offset estimations vs. SNR obtained from simulations.

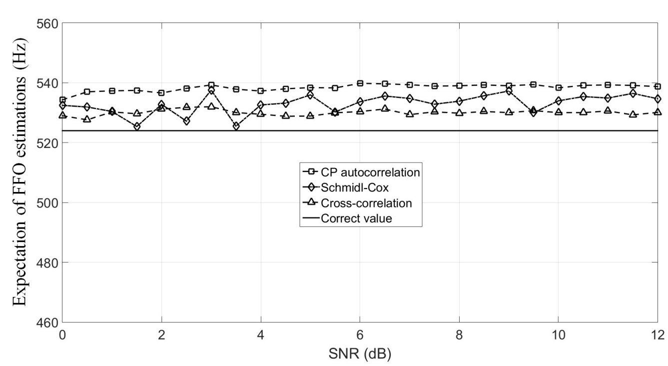

Figure 4.5: Expectation of FFO estimations vs. SNR obtained from simulations. The correct value is marked by the continuous line.

FFO values are estimated based on the timing achieved beforehand, so errors in timing synchronization also lead to errors in FFO estimation. It can be seen that some biases are introduced because of multipath. For CP autocorrelation this bias reaches approximately 16 Hz.

The standard deviations of the estimations are plotted in Figure 4.6 and show that the Schmidl-Cox method has the highest errors because the timing is estimated with some uncertainty. The cross-correlation and CP autocorrelation methods have similar precision. For example, at a SNR of 3 dB, the standard deviation is 50 Hz for both methods.

4.2 A novel ISL synchronization algorithm

In this section the time-frequency synchronization technique that was developed for one of the projects that I participated in during the doctoral studies (Hybrid-ISL) is presented [14]. The main advantages of this technique compared to common synchronization schemes is that fine timing synchronization can be achieved without a coarse stage and frequency-domain IFO estimation is not required.

The developed technique is based on cross-correlation. The approach to overcome its sensitivity to CFO is to perform the cross-correlation between the received

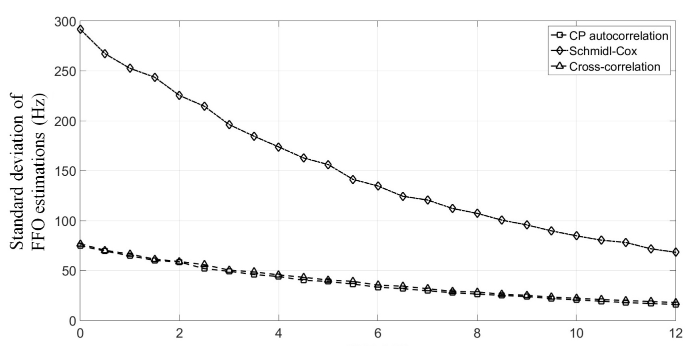

Figure 4.6: Standard deviation values of FFO estimations vs. SNR obtained from simulations.

signal $y[n]$ and several replicas of the training symbol $x_i[n]$ that incorporate CFO values considering the maximum deviation between transmitter and receiver oscillators. The cross-correlation is recalculated untill the cross-correlation peak exceeds a preset threshold. This approach leads to fine timing and coarse FFO estimation.

Since the true CFO is not guaranteed to match the discreet values in $x_i[n]$, the approach for estimating the remaining offset is to transmit two identical training symbols in the preamble. Thus, the timing metric will show two peaks corresponding to each of the symbols at Δn_1 and $\Delta n_2 = \Delta n_1 + N + N_{cp}$, respectively. Assuming that the channel is slow-varying, the autocorrelation of the received preamble is used in order to improve the accuracy of the CFO estimation in multipath conditions.

Let the remaining CFO be Δf_c^r. After timing synchronization and coarse CFO correction, the two symbols in the preamble are of the following form:

$$y_l[n] = (x[n] * h[n])e^{j2\pi \frac{\Delta f_c^r}{F_s}[n+(l-1)(N+N_{cp})]} + w_l[n] \tag{4.3}$$

where $l = 1, 2$ is the symbol index and $h[n]$ are the slow-varying channel coefficients. Δf_c^r can be estimated by measuring the phase of the autocorrelation:

$$\widehat{\Delta f_c^r} = \frac{F_s}{2\pi(N + N_{cp})} angle\left\{ \sum_{n=0}^{N-1} y_1^*[n] \cdot y_2[n] \right\} \tag{4.4}$$

4.2.1 Simulation results

In this section the proposed synchronization method is evaluated by simulations under MATLAB and is compared with the Schmidl-Cox and the CP-based autocorrelation techniques in terms of CFO estimation accuracy. The signal parameters are chosen to be in accordance with the LTE 10 MHz signal. The timing offset is set at 10^5 samples and the CFO at 21 kHz. 5000 runs are carried out at each SNR value.

The mean-squared error (MSE) of the CFO estimations for the three techniques are plotted in Figure 4.12. It can be seen that at low SNR values the CP autocorrelation gives the least accurate results. This is because the timing estimation for this method is only coarse, which in turn leads to higher errors in the CFO (more specifically FFO) estimation. At higher SNR values, the accuracy of CP autocorrelation is similar to Schmidl-Cox. The figure shows that the proposed method gives the lowest MSE. This is due to the fine timing offset estimation achieved by cross-correlation. For example, at a SNR of 0 dB, the MSE of the proposed method is 85 Hz, compared to 267 Hz for Schmidl-Cox.

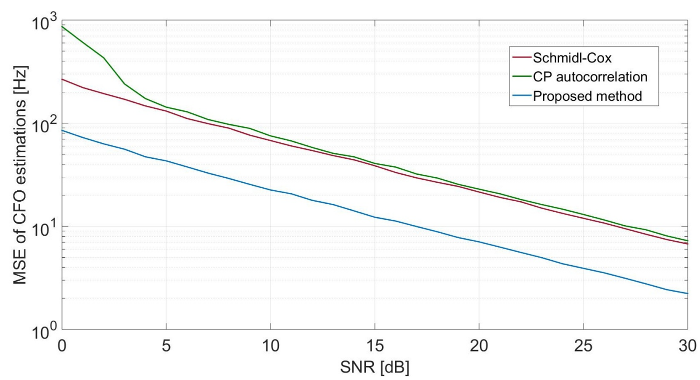

Figure 4.12: MSE of CFO estimations in AWGN channel obtained from simulations.

Chapter 5

The ISL experimental testbed

In this chapter the experimental testbed that was developed during the doctoral studies is presented. The testbed provided the means for the practical implementation of the ISL and the validation of the techniques that I developed during the doctoral program.

The main hardware elements of the testbed are Universal Software Radio Peripheral (USRP) 2952R platforms [17]. The ISL is implemented by programming the field-programmable gate arrays (FPGA) of the USRPs and a host PC application. My contributions to the ISL testbed design are:

- Preamble generation and radio frame assembly;
- Implementation of ISL time and frequency synchronization;
- Implementation of metrology techniques;
- Design of several experiments for algorithm validation.

5.1 ISL testbed design

The ISL testbed was designed in the context of an autonomous formation consisting of two spacecraft, the Master Satellite (MS) and the Slave Satellite (SS) (Fig. 5.3). The MS has the role of establishing and coordinating the data link, while the SS acts as a relative positioning reference. The measurements required for relative positioning estimation (distance and LoS) are performed at the MS. The MS also provides the time base for the ISL, thus time and frequency synchronization is performed at the SS.

The simplified block diagram of the implemented ISL is shown in Figure 5.4. The green and orange colors illustrate processing done only at the master or slave, respectively.

The entire ISL system is programmed in LabVIEW Communications. On the transmitter side, the host PC generates the baseband frequency-domain samples corresponding to an entire radio frame and sends them through a First-In-First-Out (FIFO) queue via a PCIe interface towards the USRP's FPGA. When the PC application is launched, the preamble sub-carriers are read from a file and are stored

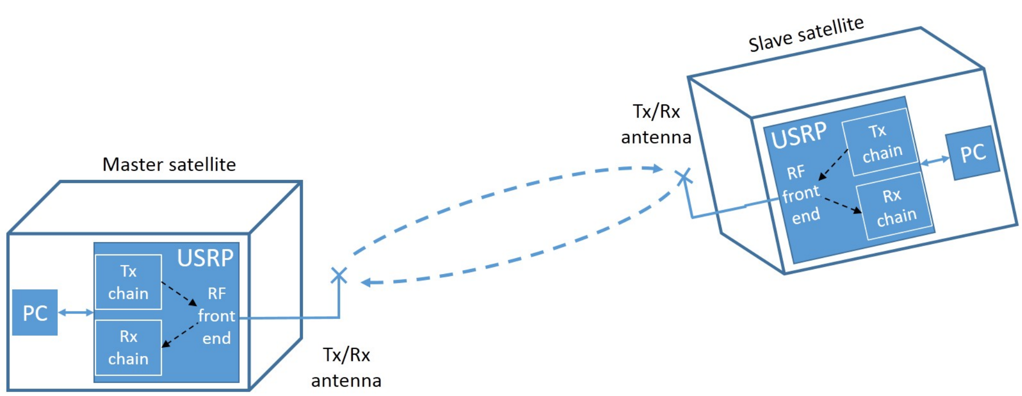

Figure 5.3: Representation of the satellite formation for the ISL testbed. The Master Satellite is the formation coordinator and the Slave is the relative positioning reference.

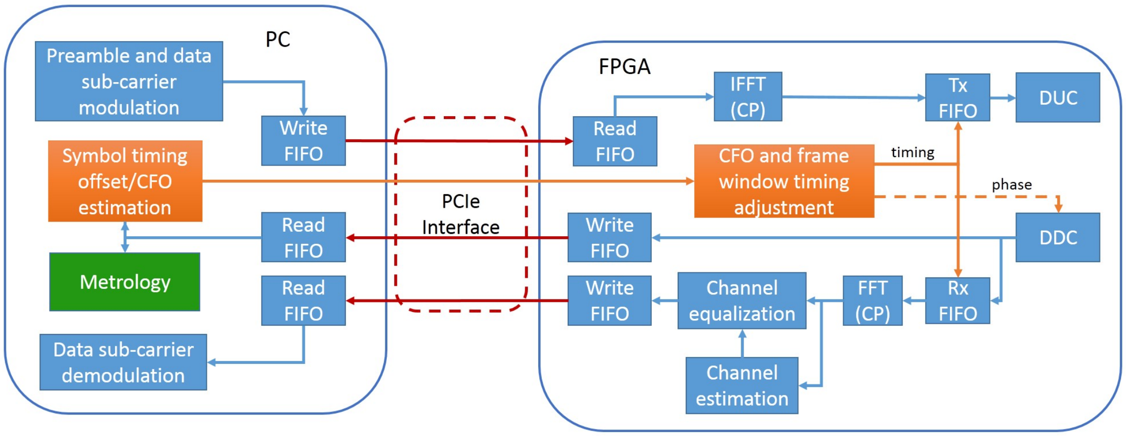

Figure 5.4: Simplified block diagram of the ISL implementation.

so that they can be appended to the beginning of each radio frame. On the FPGA, the IFFT is performed on a symbol-by-symbol basis and the CP is added to each symbol. The time-domain samples are transferred to the digital up-converter (DUC) using another FIFO.

On the receiver chain, the digital I/Q samples of the time-domain signal are transferred to the host. At the SS, these samples are used to estimate the symbol timing and CFO. The estimated values are sent back to the FPGA in order to adjust the frame timing and the phase of the received signal. The frequency of the onboard oscillator of the USRP cannot be adjusted software, only a digital phase correction can be performed in the digital down-converter (DDC). After timing and CFO have been adjusted, the received symbols are subject to CP discarding and FFT computation, followed by channel estimation and equalization. The equalized sub-carriers are transferred to the PC for data demodulation. At the MS, the time-domain samples of the received preamble are used for metrology. The second branch of the receiver chain (CP discarding, FFT, channel estimation and equalization) is the same for both master and slave, with the exception of timing adjustment at the slave.

5.1.1 Communication protocol

The ISL is implemented using Time Division Duplexing (TDD) with a radio frame structure of 10 ms as shown in Figure 5.5. The frame is divided in two equal subframes. The first one is the Downlink (DL), used to send data from the master to the slave, the other one is the Uplink (UL) reserved for sending data in the reverse sense. The Transmit/Receive Transition Gap (TTG) and the Receive/Transmit Transition Gap (RTG) are set to 5.2 µs, long enough to accommodate the round trip delay.

The FFT size used for OFDM modulation is 512 and the length of the CP is 36 samples, leading to a total symbol length of 548 samples. Each symbol is formed by modulating the innermost 300 sub-carriers with data (the DC is not modulated) and reserving the lower 106 and upper 105 sub-carriers as guard bands. The data sub-carriers are QPSK-modulated. The sampling frequency is set to 7.68 MHz, which leads to a total of 70 symbols for each subframe. The subframes start with a preamble consisting of two identical symbols. The DL and UL use different symbols.

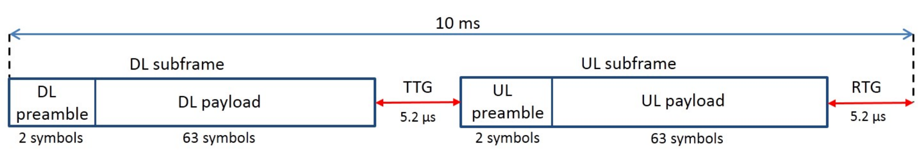

Figure 5.5: Structure of the radio frame used in the ISL implementation.

Chapter 6

ISL angle-of-arrival estimation

Using the ISL for metrology formed the basis of one of the research projects that I was involved in, HybridNAVCOM. The design of an OFDM hybrid communication-navigation system was first addressed in our paper [18] that presents the preliminary results of the ISL implementation.

This chapter presents the AoA estimation technique that I developed during the doctoral program. The proposed method represents one of the main original contributions of the thesis and is dedicated to OFDM ISLs. In the proposed approach the OFDM preamble that serves to synchronize the ISL in time and frequency and to estimate the channel impulse response is also used to obtain the AoA. The AoA is estimated by measuring the correlation of the preambles received by a couple of antennas.

The idea of using the preamble for AoA measurement was published in our paper [20], in which an analytical expression for AoA is derived and the basic estimation method is presented. Our journal paper [21] extends the previous work by improving the precision of the AoA estimate by an order of magnitude and analyzing the impact of several factors on the precision: sampling frequency, receiver noise, FFT size, CFO and multipath propagation.

6.1 System model for AoA measurement

The simplified AoA measurement model requires one transmission antenna Tx at the slave satellite and two receiver antennas at the master satellite, Rx1 and Rx2. For a planar wavefront (Figure 6.2), a simplified equation can be obtained for the AoA α:

$$\alpha = arcsin\frac{d_2 - d_1}{2r} \tag{6.1}$$

The relative LoS is a more complex task that demands the measurement of AoA in different planes. A solution can be the triplet method, which requires two orthogonal antenna rows, each row consisting in two receiver antennas (Fig. 6.4) [19]. One row is used to estimate the pitch angle while the other estimates the yaw angle.

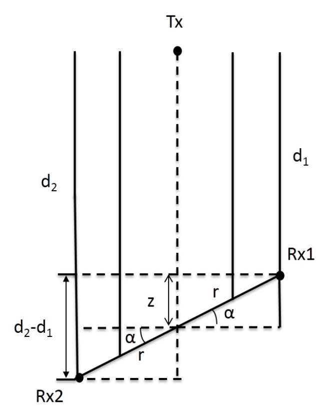

Figure 6.2: Flight formation geometry for a planar wavefront.

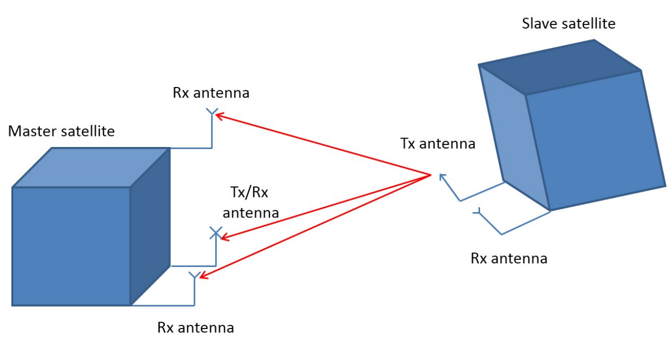

Figure 6.4: Representation of the antenna triplet. The master satellite estimates the relative orientation using the signals received by the three antennas.

6.1.1 Path difference estimation by correlation measurement

The path difference $d_2 - d_1$ can be estimated by measuring the correlation between the signals received by the two antennas Rx1 and Rx2.

The time domain correlation of the received OFDM training symbols at perfect superposition ($\tau = 0$) is:

$$R(\tau) = |X|^2 e^{j2\pi(d_2-d_1)\frac{F_c}{c}} \sum_{k=-\frac{N}{2}}^{k=\frac{N}{2}-1} e^{j2\pi\frac{k}{N}[\frac{d_2-d_1}{c}F_s+\frac{\tau}{T}]} \tag{6.2}$$

where F_c is the carrier frequency, F_s is the sampling frequency and $T = 1/F_s$. The correlation phase is given only by the exponential in front of the sum:

$$\phi_{max} = 2\pi(d_2 - d_1)\frac{F_c}{c} \tag{6.3}$$

and the following approximation can be obtained for α:

$$\alpha \approx arcsin\Big(\frac{\lambda_c}{4\pi r}\phi_{max}\Big) \tag{6.4}$$

6.1.2 Phase ambiguity resolution

If the half-wavelength condition is not satisfied [22] the path difference measurement is affected by ambiguity. A potential solution to resolve this issue is to transmit two OFDM signals with the central frequencies F_{c1} and F_{c2}. With this configuration instead of considering the phase ϕ_{max} of a single channel, one measures the *wide-lane* phase instead: $\phi_{max,wl} = \phi_{max,F_{c2}} - \phi_{max,F_{c1}}$ [23].

The disadvantage of the wide-lane technique is its sensitivity to noise. In order to improve the precision of the estimation, I developed the Half-Cycle Rounding (HCR) method. HCR is based on the observation that the true path difference $\widehat{d_2 - d_1}$ is composed of a fractional number of half-cycles measured from the cross-correlation phase and an integer number of half-cycles M that is unknown. Since the wide-lane measurement is not affected by ambiguity, the following equation can be obtained:

$$(\widehat{d_2 - d_1})_{F_{wl}} = M_2\frac{\lambda_2}{2} + (\widehat{d_2 - d_1})_{F_{c2},a} \tag{6.5}$$

In the HCR approach, the integer M_2 is estimated from (6.5) as follows:

$$\widehat{M_2} = round\left[\frac{(\widehat{d_2 - d_1})_{F_{wl}} - (\widehat{d_2 - d_1})_{F_{c2,a}}}{\frac{\lambda_2}{2}}\right] \tag{6.6}$$

and the true path difference can be obtained:

$$(\widehat{d_2 - d_1})_{F_{c2}} = M_2\frac{\lambda_2}{2} + (\widehat{d_2 - d_1})_{F_{c2,a}} \tag{6.7}$$

Table 6.2 shows the variance of M_2 calculated for $F_{c1} = 1.1$ GHz, $F_{c2} = 1.2$ GHz, $r = 18.75$ cm and σ^2 corresponding to a SNR of 10 dB. After HCR the variance of M_2 becomes practically zero, meaning that the unambigous wide-lane estimation of path difference becomes as precise as the ambigous estimation on a single channel.

6.2 Other sources of errors

In addition to AWGN, the other sources of errors in AoA estimation are the CFO, oscillator phase noise and multipath propagation. Simulations have demonstrated that the residual CFO and phase noise lead to negligible errors. The ionospheric delay does not impact the proposed technique since the AoA measurement is based on path difference estimation of the received signals. Furthermore, the change in AoA due to ionospheric scintillation is also negligible [11].

In the case of ISLs, the main sources of multipath propagation are the reflections of the RF signal on the structure surrounding the antennas. The error can be up to several cm in path difference and could lead to ambiguity resolution failure and degradation of accuracy [24].

Table 6.2: Estimator variance at 10 dB

σ^2	$\sigma^2_{F_{c2}}$	σ^2_{wl}	$\sigma^2_{M_2}$	$\sigma^2_{[M_2]}$	$\sigma_\alpha[°]$
$2.1e-4$	$3.3e-7$	$9.5e-5$	$5.6e-3$	≈ 0	0.088

6.3 Experimental results

In this section, part of the theoretical considerations regarding the AoA estimation are validated by tests on an ISL implemented in real-time using the USRP platforms.

6.3.1 The ISL setup

The setup consists in three USRP platforms, as seen in Figure 6.12. USRP1 and USRP2 are used to implement the master satellite and USRP3 is reserved for the slave satellite. The cables that connect the receiver antennas to the USRPs are of equal length. The ISL is implemented using the TDD frame structure described in Chapter 5. The carrier frequencies are $F_{c1} = 1.1$ GHz and $F_{c2} = 1.2$ GHz, whose combination leads to $\lambda_{wl} = 3$ m.

For the purpose of the real-time measurements, the reference frequency is generated by an Octoclock [25] and is provided to all three USRPs using coaxial cables.

The antennas of the master satellite are mounted on a tripod with a rotatable surface on top. The rotation can be performed with a step of $2°$ in the range $[-30°, +30°]$. The distance between Rx1 and Rx2 is 37.5 cm, meaning that λ_{wl} fulfils the half-wavelength condition. All antennas are placed at the same height.

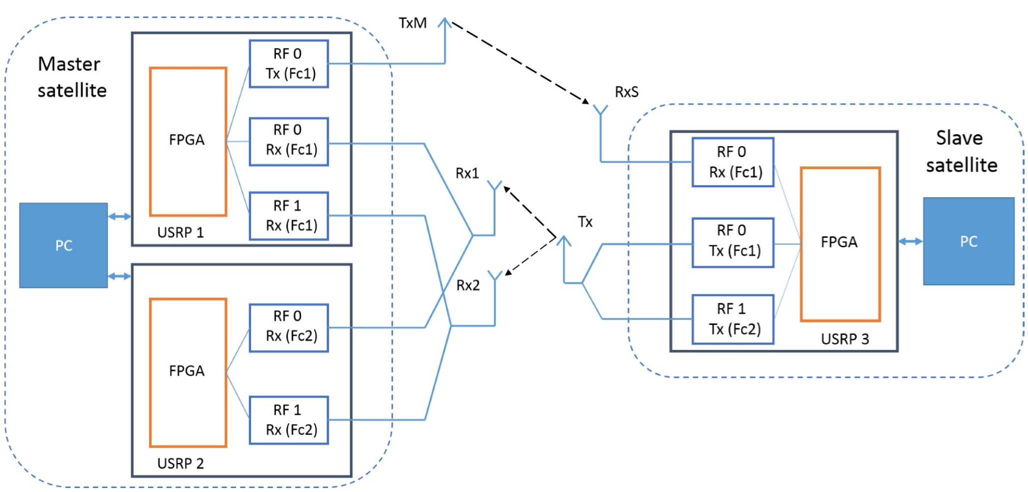

Figure 6.12: Diagram of the AoA experimental setup.

6.3.2 Results on measured data

Figure 6.15 depicts the angles estimated with the basic wide-lane technique at 26 dB. For the same phase measurements, the angles estimated by HCR are shown in Figure 6.16. In the second plot, the dots are much closer to the ideal straight-line, showing a more accurate estimation.

In the second experiment, with α set at $10°$, the transmit power at the slave is varied such to obtain 10 different SNRs and 5000 measurements are recorded for each SNR. The standard deviation values plotted in Figure 6.17 show that the real-time results are close to the simulated values, aiding in the validation of the proposed approach. The precision provided by HCR remains more than one order of magnitude better than that obtained by the the wide-lane technique. At a SNR of 30 dB the precision is improved from $0.193°$ to $0.013°$.

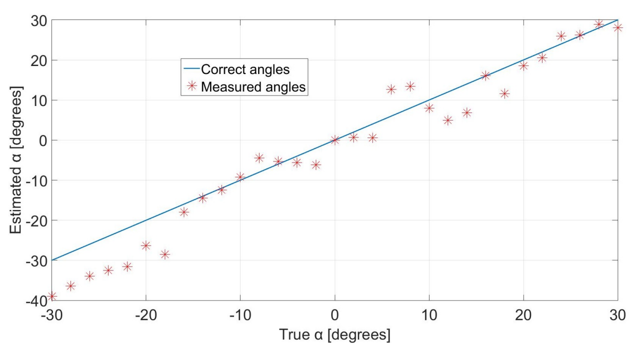

Figure 6.15: AoA estimated with the wide-lane technique and real-time measurements at SNR = 26 dB. The correct angles are represented by the full line.

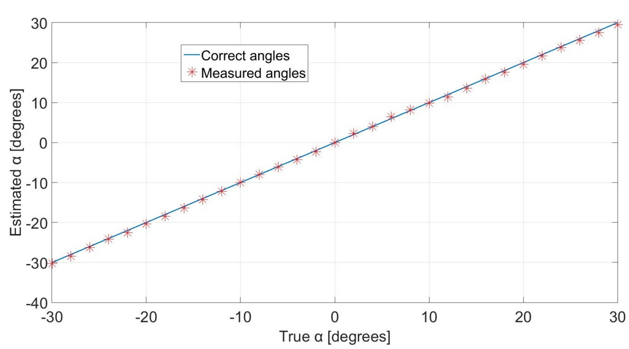

Figure 6.16: AoA estimated by HCR from real-time measurements at SNR = 26 dB. The correct values of the angles are represented by the full line.

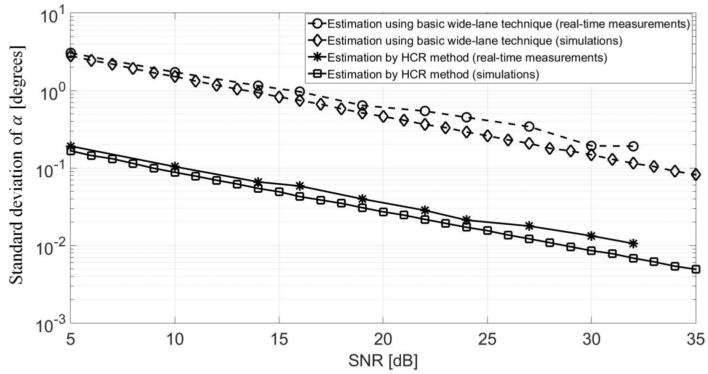

Figure 6.17: AoA standard deviation with real-time measurements (dotted lines) and by simulations (solid lines).

Chapter 7

Inter-satellite distance estimation

In the case of OFDM signals, distance estimation can be done in frequency-domain or time-domain. Regarding frequency-domain estimation, the main contributions of the doctoral research consist of the following:

1. Performing a comparison between two OFDM ranging techniques, the repeater and frequency correlation methods, with the purpose of identifying an approach suitable for future space missions [26]. The investigated methods rely on transmitting a training symbol (preamble) and exploit the frequency-domain properties of OFDM to estimate the inter-satellite distance.

2. Proposing an improvement for the frequency correlation method that increases the accuracy almost twofold at low SNR values [27]. The improvement is based on processing multiple symbols that are received simultaneously by the antennas of the relative LoS system presented in Chapter 6.

The major contribution of the thesis regarding satellite ranging is represented by the development of a time-domain distance estimation technique called Enhanced Wide-Lane (EWL). EWL is associated with ISL timing synchronization and is based on obtaining a coarse estimation that is refined using phase measurements. EWL was developed as part of the HybridNAVCOM project and was published in the journal paper [28].

7.1 The repeater method

In the repeater method [29] the slave satellite receives a training symbol from the master and acts as a repeater: after a fixed processing delay, it retransmits the training symbol back to the master. When the training symbol arrives back at the master, the roundtrip delay of the signal can be estimated. First, a coarse delay is calculated by time-domain cross-correlation. Then, the estimation is refined in the frequency domain from the phase shifts of the received sub-carriers [29].

7.2 The frequency correlation method

In the frequency correlation method, the distance d is estimated entirely from the phase shifts of the received sub-carriers. The received symbol is represented in the frequency-domain, its autocorrelation is computed and a differential sequence is calculated in order to remove the phase ambiguities [30].

The bandwidth of the transmitted signal strongly influences the precision of the frequency correlation method (through the sub-carrier spacing F_s/N), along with the number of modulated sub-carriers in the training symbol. The first line in Table 7.1 shows the standard deviation values of the distance estimations for several channel bandwidths corresponding to an LTE signal and a SNR of 20 dB. The results show that the precision is better than 1 cm when the channel bandwidth is 20 MHz.

7.3 Improvement of the frequency correlation method

The values in Table 7.1 show that a reduced signal bandwidth results in a significant loss in precision. I have proposed an improvement of the method that consists in performing linear regression on the estimated phases of the received sub-carriers after unwrapping them. With this approach the true distance d can be estimated with higher precision. The results in Table 7.1 (line 2) show that for a channel bandwidth of 5 MHz the precision is improved from 14.3 to 11.6 cm after linear regression. Furthermore, regression on the three signals received simultaneously by the antenna triplet of the relative LoS subsystem (Fig. 6.4) significantly improves the precision of the distance estimate. Table 7.1 shows that the precision is improved from 11.6 to 6.9 cm when using all of the available signals for regression.

7.3.1 Experimental results for linear regression

In this section the impact of linear regression on the accuracy of the distance estimation is analyzed using testbed measurements. The system parameters are equivalent to an LTE signal with a bandwidth of 5 MHz. The satellites are considered frequency-aligned. The carrier frequency is $F_c = 1.2$ GHz and the distance is $d = 4.6$ m.

The block diagram of the USRP testbed used for real-time measurements is depicted in Figure 7.9. Each platform uses the radio frequency channel RF0 and is tuned

Table 7.1: Standard deviation [cm] at 20 dB

Channel bandwidth [MHz]	3	5	10	20
Frequency Correlation	38.09	14.34	5.01	1.81
Regression on 1 symbol	35.66	11.64	4.11	1.48
Regression on 3 symbols	20.97	6.91	2.41	0.87

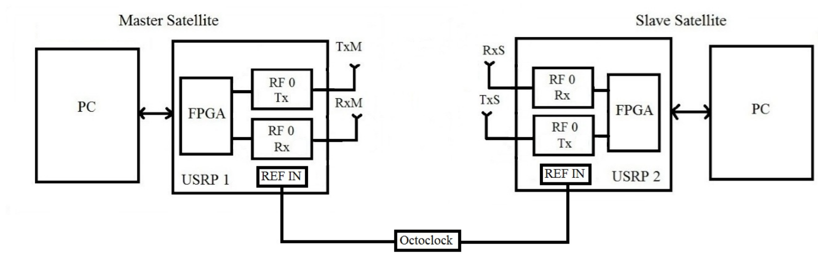

Figure 7.9: Diagram of the experimental setup: the Master Satellite is implemented on USRP 1, while the Slave Satellite is implemented on USRP 2.

at $F_c = 1.2$ GHz. The master satellite is implemented on USRP 1 and performs the distance estimations and the slave is implemented on USRP 2. The Octoclock device provides the reference frequency. Since only one receiver antenna was mounted on the master satellite, the regression was done on a single symbol. The estimated distance was that from TxS to RxM.

Figure 7.10 shows the expectation of the estimations. It can be seen that the estimations are not biased. The standard deviations of the frequency correlation and improved estimations are plotted in Fig. 7.11. The testbed measurements show that linear regression improves the distance estimation precision. For example, at 28 dB, linear regression leads to an increase in precision from 7.1 cm to 5.2 cm.

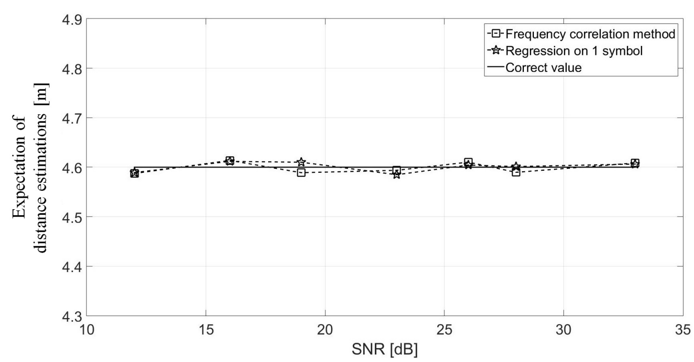

Figure 7.10: The expectation of distance estimates vs. SNR obtained from real-time measurements in the cases of basic frequency correlated method and our improved version (regression on a single symbol).

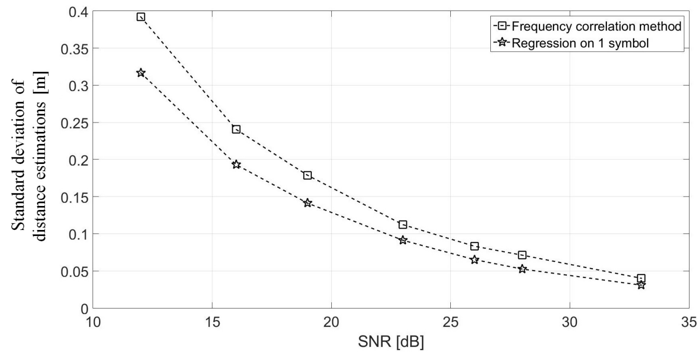

Figure 7.11: The standard deviation of the distance estimators vs. SNR obtained from real-time measurements.

7.4 The Enhanced Wide-Lane method

In this section a cross-correlation based technique called the Enhanced Wide-lane Method (EWL) is proposed [28]. The method is associated with ISL timing synchronization and is based on obtaining a coarse estimation that is refined using phase measurements. EWL was developed as part of the HybridNAVCOM project.

The EWL technique is based on calculating the cross-correlation of the received training symbol $y(t)$ with the locally stored replica $x(t)$. The sampling frequency F_s imposes a resolution of $\delta d = c/F_s$ in measuring the distance. For instance, at $F_s = 7.68$ MHz, this resolution is approximately 39 m meaning a maxim error of 19.5 m. Thus, detecting the maximum of correlation provides only a coarse estimation $\hat{d}_{coarse}$.

More accurate information about the distance can be obtained from the phase of the cross-correlation. Similar to the technique described in Chapter 6, the distance can be derived from the cross-correlation phase ϕ_{max}:

$$d = \frac{c}{2\pi F_c}\phi_{max} = \frac{\lambda_c}{2\pi}\phi_{max} \tag{7.1}$$

In order to improve the resolution δd, the cross-correlation is computed for over-sampled versions of the signals x and y. Moreover, the timing synchronization of the

ISL must also be considered. The EWL method imposes that timing synchronization and signal oversampling for coarse distance estimation be performed at the same frequency. Consider the TDD frame depicted in Figure 7.14. At the master satellite (MS), the timing is fixed. For a certain distance d, the delay of the DL signal due to propagation (trip delay) is Δx samples (Fig. 7.14, top). In the ISL synchronization process, the slave satellite (SS) adjusts its timing such that the beginning of the radio frame corresponds to the first sample in the DL signal. Then, it transmits the UL after exactly 5 ms. At the MS, the delay of the UL becomes $2\Delta x$ samples (proportional to the round trip delay). Considering the same value for F_s and an oversampling factor of 8, when d increases by 2.441 m, the delay of the DL becomes $\Delta x + 1$ samples and the delay of the UL seen at the MS is now $2\Delta x + 2$ samples (Fig. 7.14, bottom). The detected increase in distance would be 4.882 m, therefore a division with 2 is necessary in order to estimate the correct value of d_{coarse}.

The second aspect of EWL consists in transmitting the training symbol on a second channel and taking the wide-lane phase ϕ_{wl}. The two carrier frequencies must be chosen such that $\lambda_{wl} \geq \delta d$.

The unambiguous estimation of d also requires the knowledge of the number of

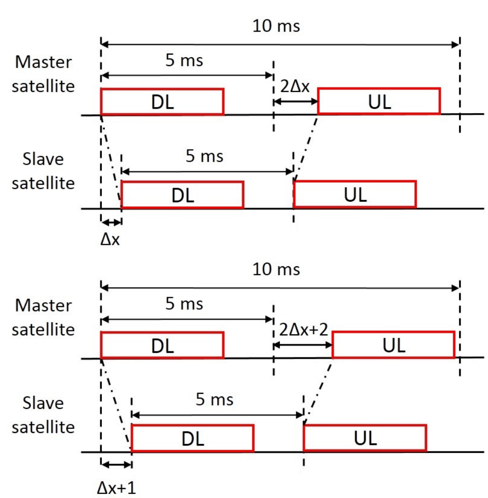

Figure 7.14: Radio frame timing used for coarse distance estimation when the inter-satellite distance is d (top) and $d + 2.441$ m (bottom).

wide-lane cycles N_{wl} traveled by the signal between the satellites:

$$d_{wl} = (N_{wl} + \frac{\phi_{wl}}{2\pi})\lambda_{wl} \tag{7.2}$$

N_{wl} can be estimated from $\hat{d}_{coarse}$ by [31]:

$$\hat{N}_{wl} = round\Big(\frac{\hat{d}_{coarse} - \lambda_{wl}\phi_{wl}/2\pi}{\lambda_{wl}}\Big) \tag{7.3}$$

The precision of the distance estimation can be improved by solving the ambiguity for a single frequency:

$$\hat{N}_{F_{c2}} = round\Big(\frac{\hat{d}_{wl} - \lambda_{c2}\phi_{max,F_{c2}}/2\pi}{\lambda_{c2}}\Big) \tag{7.4}$$

and computing the distance:

$$\hat{d}_{fine} = (\hat{N}_{F_{c2}} + \phi_{max,F_{c2}}/2\pi)\lambda_{c2} \tag{7.5}$$

7.4.1 Effects of frequency misalignment and multipath

Computer simulations have shown that for residual CFO values up to 150 Hz, the equivalent distance estimation error is maximum 1.27 mm. The SFO introduces negligible errors.

The phase biases caused by multipath could lead to errors of up to several meters when the order of ambiguity is incorrectly estimated. Even with multipath compensation by anechoic chamber measurements, in cases when the fractional part of the ambiguity order is close to 0.5 even small biases could lead to large errors. For this reason filtering would be necessary in order to discard the erroneous estimations.

7.4.2 Experimental results

In this section the EWL method is evaluated with the USRP 2952R testbed. The ISL signal parameters are the same as in Chapter 6. The transmit power is varied to obtain several SNR values and 5000 measurements are recorded at each SNR.

The block diagram of the real-time testbed is shown in Figure 7.20. The refer-

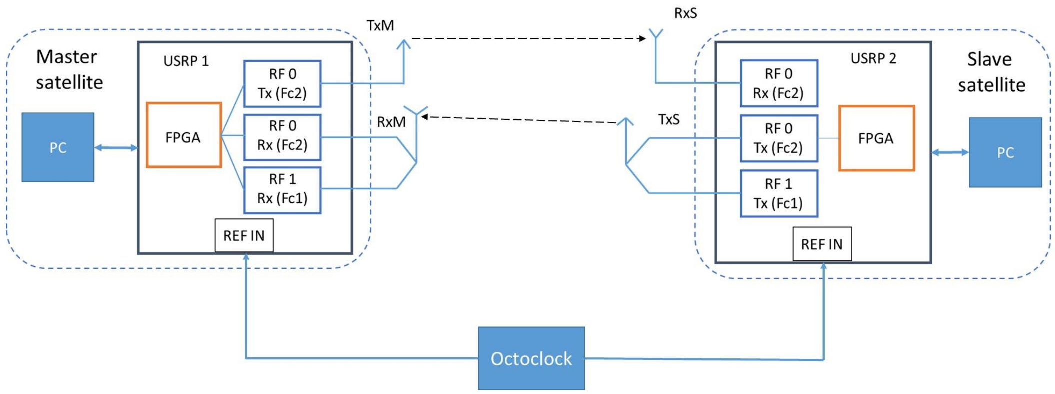

Figure 7.20: Diagram of the experimental setup: the Master Satellite is implemented using on USRP 1, while the Slave Satellite is implemented on USRP 2.

ence frequency is generated by the Octoclock and is provided to both USRPs. The measured distance is from TxS to RxM.

The mean values of the estimations versus SNR are depicted in Figure 7.22. The plots are close to 4.6 m level for both d_{wl} and d_{fine}, showing a non biased estimation.

The standard deviations are plotted in Figure 7.23 and show consistent improvements in precision for the considered SNR range. At 28 dB SNR, the precision is improved from 1 mm to 0.07 mm. A similar improvement was also obtained by simulations (from 0.8 to 0.05 mm).

A second experiment was performed in order to verify that the precision of $\hat{d}_{fine}$ is improved for lower values of λ_{c2} (higher carrier frequencies). For this purpose, phase

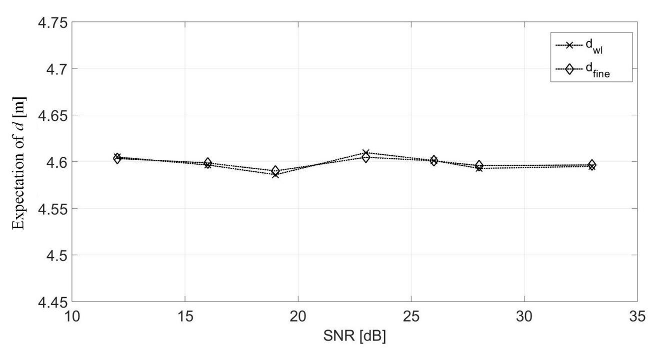

Figure 7.22: Expectation values of the estimations vs. SNR obtained from real-time measurements.

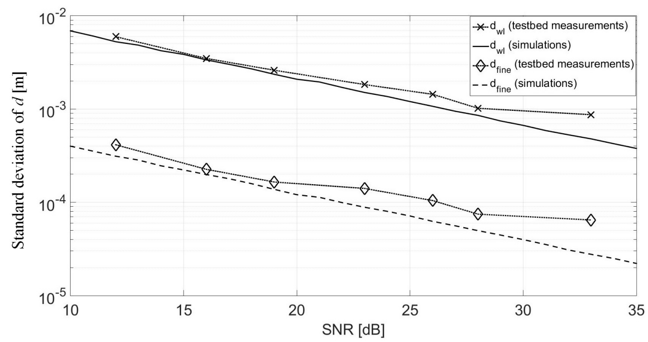

Figure 7.23: Standard deviation of the EWL method vs. SNR obtained from testbed measurements and simulations.

measurements were conducted for two other carrier frequencies: $F_{c2} = 1.7$ and 2 GHz ($\lambda_{c2} = 17.64$ and 15 cm). The obtained standard deviations are plotted in Fig. 7.24. They show that by reducing λ_{c2}, the precision of the estimation improves at low SNR values. For example, at a SNR of 12 dB, the estimator standard deviation is 0.34 mm for $\lambda_{c2} = 17.64$ cm and 0.3 mm for $\lambda_{c2} = 15$ cm. At high SNR values, decreasing the wavelength leads to a negligible precision improvement.

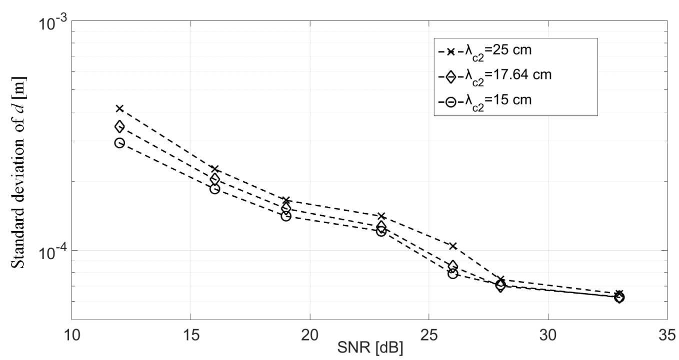

Figure 7.24: Standard deviations of EWL estimator for various values of the wavelength λ_{c2}.

Chapter 8

Conclusion

This thesis presents research and experiments performed in order to develop novel RF ISL synchronization and metrology techniques for autonomous satellite missions. For this purpose, the thesis begins by presenting the state-of-the-art existing solutions for satellite formation flying. Based on the examined literature, a dual communication-metrology approach is proposed, such that the ISL is used also for relative positioning estimation. The advantages of this approach consist in cost and energy expenditure reduction, at the price of a decrease in positioning accuracy compared to optical metrology systems.

OFDM is employed as waveform for the ISL considering its many advantages, such as robustness against fading, efficient implementation by FFT and simple channel equalization.

This thesis proposes a complete solution for relative positioning estimation of formating flying satellites. Line-of-Sight and distance estimation are treated in a unitary manner and integrated in a metrology system that functions based on the same principles. More specifically, an OFDM training symbol is transmitted on two carrier frequencies and relative positioning is estimated by correlation phase measurements. Since the metrology system is RF based and uses the ISL, data link synchronization also had to be addressed. We proposed a novel synchronization technique based on cross-correlation between the received signal and local replicas of the OFDM training symbol that encompass various carrier frequency offsets. The results in the thesis show that the RF solution is viable and that the performances of RF metrology systems can approach those of optical or hybrid systems, which have higher accuracy but are more costly in terms of energy, satellite mass and volume.

The proposed solutions have been thoroughly examinated in the thesis by theoretical analysis. The theory was first verified using a dedicated MATLAB simulator, then validated using a specially developed USRP testbed. Special consideration was given to the case in which the satellites are close, or in other words for high SNR values. The precision of distance and AoA estimation obtained from testbed measurements was 0.07 mm (SNR of 28 dB) and 0.013° (SNR of 30 dB), respectively. The original contributions of the thesis are presented in detail in the next section.

The work in this thesis was conducted in tandem with two research projects, HybridNAVCOM and Hybrid-ISL. Part of the algorithms developed in the thesis were tested and validated at the GMV Advanced Robotics Testbed in Madrid, Spain.

8.1 Original contributions

The original contributions developed in this thesis, referred to the published research papers, are as follows:

- The comparison of several time and frequency synchronization techniques for OFDM signals, with the purpose of identifying a suitable approach for ISLs (conference paper [13]);
- The development of a concept design of a dual communication-navigation system (conference paper [18]);

- The development of a joint time-frequency synchronization algorithm based on blind frequency offset estimation (conference paper [14]);
- The development of an AoA estimation technique that is used to derive the relative Line-of-Sight between satellites (conference paper [20] and journal paper [21]);
- The comparison of two frequency domain distance estimation methods for OFDM and the development of an improvement for one of the considered methods (conference papers [26] and [27]);
- The development of an inter-satellite distance estimation technique for OFDM ISLs (journal paper [28]).

8.2 List of published papers

8.2.1 Journal papers

1. A. M. Crisan, A. Martian, R. Cacoveanu and D. Coltuc, "Angle-of-Arrival Estimation in Formation Flying Satellites: Concept and Demonstration," in *IEEE Access* (IF 4.098, quartile Q1), vol. 7, pp. 114116-114130, 2019. doi: 10.1109/ACCESS.2019.2935620. WOS: 000483022100060
2. A. M. Crisan, A. Martian, R. Cacoveanu and D. Coltuc, "Distance estimation in OFDM inter-satellite links," in *Measurement* (IF 2.791, quartile Q2), vol. 154, March 2020. ISSN 0263-2241, doi: 10.1016/j.measurement.2020.107479. WOS: 0005170886000026

8.2.2 Conference papers

1. A. Crisan, A. Martian, R. Cacoveanu and D. Coltuc, ”Evaluation of synchronization techniques for inter-satellite links,” in *2016 International Conference on Communications (COMM)*, Bucharest, Romania 2016, pp. 463-468 (ISI indexed IEEE Conf.). doi: 10.1109/ICComm.2016.7528259. WOS: 0003832219000094

2. P. Bajanaru, C.C. Chitu, R. Cacoveanu, A.M. Crisan and A. Martian, ”Design and development of a satellite on-board communication system with navigation capabilities,” in *67th International Astronautical Congress (IAC)*, Guadalajara, Mexico, 2016.

3. A. Crisan, A. Martian and D. Coltuc, ”Relative orientation estimation in formation flying satellites,” in *2017 International Symposium on Signals, Circuits and Systems (ISSCS)*, Iasi, Romania, 2017, pp. 1-4 (ISI indexed IEEE Conf.). doi: 10.1109/ISSCS.2017.8034927. WOS:000517088600026

4. A. Crisan, ”Inter-Satellite Radio Frequency Ranging Techniques for OFDM Communication Systems,” in *2018 International Conference on Communications (COMM)*, Bucharest, 2018, pp. 391-394 (ISI indexed IEEE Conf.). doi: 10.1109/ICComm.2018.8484801. WOS: 000425211500065

5. A. Crisan, A. Martian and D. Coltuc, ”Inter-Satellite Radio Frequency Ranging in a Hybrid OFDM Communication-Metrology System,” in *2018 15th Workshop on Positioning, Navigation and Communications (WPNC)*, Bremen, 2018, pp. 1-5 (ISI indexed IEEE Conf.). doi: 10.1109/WPNC.2018.8555795. WOS: 000460539800018

6. A. Crisan, C. Anghel and R. Cacoveanu, ”A Novel Synchronization Algorithm for Hybrid Inter-Satellite Link Establishment,” in *15th Advanced International Conference on Telecommunications (AICT)*, Nice, France, 2019.

8.2.3 Future work

There are several future research directions for RF communication-metrology techniques. Considering the communication aspect of the ISL, although OFDM has been extensively reasearched in the last decades, the possibility of high peak-to-average power ratio (PAPR) remains a significant impairment. The current solutions for PAPR reduction involve an increase in overall system complexity, thus it would be desired to develop efficient methods to obtain low PAPR data symbols without increasing overhead.

Another potential research direction would be inter-satellite channel impulse response modeling. In this case the satellite trajectories must be considered to account for possible fading effects such as ionospheric scintillation.

The research in this thesis has shown that multipath propagation is the main source of errors for relative positioning estimation. Future research should be oriented towards developing multipath mitigation techniques or novel relative positioning methods that achieve a compromise between complexity and robustness to multipath effects.

Bibliography

[1] https://directory.eoportal.org/web/eoportal/satellite-missions/t/tandem-x, last accessed 8 Feb. 2020.

[2] J.-S. Ardaens, S. D'Amico, D. Ulrich, D. Fischer, "TanDEM-X Autonomous Formation Flying System", in *3rd International Symposium on Formation Flying, Missions (FFMT) and Technologies*, ESA/ESTEC, Noordwijk, The Netherlands, April 23-25, 2008.

[3] J. Kim and B. D. Tapley, "Error Analysis of a Low-Low Satellite-to-Satellite Tracking Mission," in *Journal of Guidance, Control, and Dynamics*, vol. 25, no. 6 (2002), pp. 1100-1106.

[4] J. Kim and S. W. Lee, "Flight performance analysis of GRACE K-band ranging instrument with simulation data," in *Acta Astronautica*, vol. 65, issues 11-12, pp. 1571-1581, December 2009.

[5] O. Montenbruck, M. Delpech, J.-S. Ardaens, N. Delong , S. D'Amico and J. Harr, "Cross-validation of GPS- and FFRF-based relative navigation for the PRISMA Mission," in *Proceedings of NAVITEC 2008, 4th ESA Workshop on Satellite Navigation User Equipment Technologies GNSS User Technologies in the Sensor Fusion Era*, Noordwijk, The Netherlands, December 2008.

[6] M. Delpech, P. Y. Guidotti, S. Djalal, T. Grelier and J. Harr, "RF Based Navigation For PRISMA and other Formation Flying Missions in Earth Orbit," in *Advances in the Astronautical Sciences*, 2009.

[7] P. Rodrigues, R. Mendes, P. Sinogas, A. Oliveira and K. Mellab, "Enabling Inter-Satellite Link platform for multi-satellite missions," in *Proceedings of the 66th International Astronautical Congress (IAC)*, Jerusalem, Israel, October 2015.

[8] M. Speth, S. Fechtel, G. Fock and H. Meyr, "Optimum receiver design for OFDM-based broadband transmission. II. a case study," in *IEEE Transactions on Communications*, vol. 49, pp. 571–578, Apr 2001.

[9] C. Oberli, "ML-based Tracking Algorithms for MIMO-OFDM," in *IEEE Transactions on Wireless Communications*, vol. 6, no. 7, pp. 2630-2639, July 2007.

[10] M. Nassar, P. Schniter and B. L. Evans, "A Factor Graph Approach to Joint OFDM Channel Estimation and Decoding in Impulsive Noise Environments," *IEEE Transactions on Signal Processing*, vol. 62, no. 6, pp. 1576-1589, March 2014.

[11] ITU-R ionospheric propagation recommendation: https://www.itu.int/dms_pubrec/itu-r/rec/p/R-REC-P.531-11-201202-S!!PDF-E.pdf, last accessed 14 July 2019.

[12] HybridNAVCOM Scientific and Technical Report, 2016.

[13] A. Crisan, A. Martian, R. Cacoveanu and D. Coltuc, "Evaluation of synchronization techniques for inter-satellite links," in *2016 International Conference on Communications (COMM)*, Bucharest, 2016, pp. 463-468.

[14] A. Crisan, C. Anghel and R. Cacoveanu, "A Novel Synchronization Algorithm for Hybrid Inter-Satellite Link Establishment," in *15th Advanced International Conference on Telecommunications (AICT)*, Nice, France, 2019.

[15] T. M. Schmidl and D. C. Cox, "Robust frequency and timing synchronization for OFDM," in *IEEE Transactions on Communications*, vol. 45, no. 12, pp. 1613-1621, Dec. 1997.

[16] J. J. van de Beek, M. Sandell and P. O. Borjesson, "ML estimation of time and frequency offset in OFDM systems," in *IEEE Transactions on Signal Processing*, vol. 45, no. 7, pp. 1800-1805, July 1997.

[17] http://www.ni.com/ro-ro/support/model.usrp-2952.html, last accessed 16 May 2019.

[18] P. Bajanaru, C.C. Chitu, R. Cacoveanu, A.M. Crisan and A. Martian, "Design and Development of a Satellite on-Board Communication System with Navigation Capabilities," in *Proceedings of the 67th IAC (International Astronautical Congress)*, Guadalajara, Mexico, 2016.

[19] D. Niculescu and B. Nath, "Ad hoc positioning system (APS) using AOA," in *Twenty-second Annual Joint Conf. of the IEEE Comp. and Comm. Soc.*, pp. 1734-1743, vol. 3, 2003. doi: 10.1109/INFCOM.2003.1209196

[20] A.M. Crisan, A. Martian and D. Coltuc, "Relative orientation estimation in formation flying satellites," in *IEEE Int. Symp. on Signals, Circuits and Systems (ISSCS)*, pp. 1-4, 2017. do: 10.1109/ISSCS.2017.8034927

[21] A. M. Crisan, A. Martian, R. Cacoveanu and D. Coltuc, "Angle-of-Arrival Estimation in Formation Flying Satellites: Concept and Demonstration," in *IEEE Access*, vol. 7, pp. 114116-114130, 2019. doi: 10.1109/ACCESS.2019.2935620

[22] M. H. El-Shafey, T. Abdul-Rahman and Y. H. Dakroury, "Relaxing the Half-Wavelength Condition for Estimating Signal AoA at a Line of Sensors," in *16th European Signal Proc. Conf.*, pp. 1-5, Lausanne, Aug. 2008.

[23] K. O'Keefe, M. Petovello, W. Cao, G. Lachapelle and E. Guyader, "Comparing Multicarrier Ambiguity Resolution Methods for Geometry-Based GPS and Galileo Relative Positioning and Their Application to Low Earth Orbiting Satellite Attitude Determination," in *Int. Journal of Navigation and Observation*, vol. 2009, 2009. doi: 10.1155/2009/592073

[24] T. Grelier, et al., "Formation Flying RadioFrequency Instrument: First Flight Results from the PRISMA Mission," in *2010 5th ESA Workshop on Satellite Navigation Technologies and European Workshop on GNSS Signals and Signal Processing (NAVITEC)*, pp. 1-8, Noordwijk, Dec. 2010. doi: 10.1109/NAVITEC.2010.5708059

[25] Octoclock: https://www.ettus.com/product/details/ OctoClock, last accessed 5 Dec. 2018.

[26] A. Crisan, "Inter-Satellite Radio Frequency Ranging Techniques for OFDM Communication Systems," in *2018 International Conference on Communications (COMM)*, Bucharest, 2018, pp. 391-394. doi: 10.1109/ICComm.2018.8484801

[27] A. Crisan, A. Martian and D. Coltuc, "Inter-Satellite Radio Frequency Ranging in a Hybrid OFDM Communication-Metrology System," in *2018 15th Workshop on Positioning, Navigation and Communications (WPNC)*, Bremen, 2018, pp. 1-5. doi: 10.1109/WPNC.2018.8555795

[28] A. M. Crisan, A. Martian, R. Cacoveanu and D. Coltuc, "Distance estimation in OFDM inter-satellite links," in *Measurement*, vol. 154, March 2020. ISSN 0263-2241, doi: 10.1016/j.measurement.2020.107479

[29] G. Ren, C. Sun, H. Ni and Y. Bai, "OFDM-Based Precise Ranging Technique in Space Applications," in *IEEE Trans. on Aerospace and Electr. Syst.*, vol. 47, no. 3, pp. 2217-2221, July 2011.

[30] L. Dai, Z. Wang, J. Wang and Z. Yang, "Positioning with OFDM signals for the next- generation GNSS," in *IEEE Trans. on Cons. Electr.*, vol. 56, no. 2, pp. 374-379, May 2010.

[31] B. Forssell, M. Martin-Neira and R. A. Harris, "Carrier Phase Ambiguity resolution in GNSS-2," in *Proc. of ION GPS-97*, pp. 1727–1736, Kansas City, 16-19 Sept. 1997.